

Earth-Viewing L-Band Radiometer Sensing of Sea Surface Scattered Celestial Sky Radiation—Part II: Application to SMOS

Nicolas Reul, Joseph Tenerelli, Nicolas Floury, and Bertrand Chapron

Abstract—We examine how the rough sea surface scattering of L-band celestial sky radiation might affect the measurements of the future European Space Agency Soil Moisture and Ocean Salinity (SMOS) mission. For this purpose, we combined data from several surveys to build a comprehensive all-sky L-band celestial sky brightness temperature map for the SMOS mission that includes the continuum radiation and the hydrogen line emission rescaled for the SMOS bandwidth. We also constructed a separate map of strong and very localized sources that may exhibit L-band brightness temperatures exceeding 1000 K. Scattering by the roughened ocean surface of radiation from even the strongest localized sources is found to reduce the contributions from these localized strong sources to negligible levels, and rough surface scattering solutions may be obtained with a map much coarser than the original continuum maps. In rough ocean surface conditions, the contribution of the scattered celestial noise to the reconstructed brightness temperatures is not significantly modified by the synthetic antenna weighting function, which makes integration over the synthetic beam unnecessary. The contamination of the reconstructed brightness temperatures by celestial noise exhibits a strong annual cycle with the largest contamination occurring in the descending swaths in September and October, when the specular projection of the field of view is aligned with the galactic equator. Ocean surface roughness may alter the contamination by over 0.1 K in 30% of the SMOS measurements. Given this potentially large impact of surface roughness, an operational method is proposed to account for it in the SMOS level 2 sea surface salinity algorithm.

Index Terms—Microwave radiometry, sea surface electromagnetic scattering.

I. INTRODUCTION

CELESTIAL sky L-band radiation scattered by the ocean surface can contaminate spaceborne measurements of upwelling sea surface brightness temperature used to retrieve sea surface salinity (SSS). The sensitivity of the linearly polarized sea surface brightness temperature to salinity ranges from about 0.2 to 0.8 K/psu [1] (depending on ocean surface temperature, incidence angle, and polarization). Since the open ocean surface

salinity generally ranges from 32 to 37 psu, the expected dynamical range of L-band emission brightness temperatures associated with variations in SSS alone is small relative to the total brightness temperature, which is less than approximately 4 K for open ocean conditions.

For the Aquarius/SAC-D mission, it was reported in [2] that, under the assumption of a flat perfectly conducting Earth surface (with a reflectivity of 1), the total celestial sky radiation contribution to the antenna temperature varies from a little less than 4 K to more than 9 K. For a perfectly flat dielectric sea surface, the reflectivity may range from about 30% to 80% at 1.4 GHz for incidence angles below 50°, depending on the SSS, sea surface physical temperature, and observation polarization. In this case, the contamination ranges from about 1 to 7 K. As discussed in [3] (hereinafter referred to as Part I), ocean surface roughness both decreases the surface reflectivity and directionally spreads the impact of the source brightness. For specular points in the vicinity of the galactic equator, the spreading effect of the rough surface greatly reduces the impact along the equator and broadens the contamination far beyond the narrow bright source concentrated along the equator. Nevertheless, for specular points far from strong sources, sea surface roughness has a negligible impact on the reflected signal. Overall, the intensity of the scattered celestial noise ranges from approximately 30% to 70% of the flat ocean surface reflected values, with most of the variation associated with the directional spreading of the radiation.

The nonuniform distribution of celestial radiation has an important systematic impact on the measurements. The future European Space Agency Soil Moisture and Ocean Salinity (SMOS) and National Aeronautics and Space Administration/Comisión Nacional de Actividades Espaciales Aquarius/SAC-D satellites that are dedicated to SSS remote sensing will be launched in the near future into sun-synchronous orbits, and considering these orbits along with the Earth's orbit around the sun, the celestial sky glitter contamination will exhibit strong geographic and seasonal dependence. As such, flagging and correction strategies for such contamination must be developed to reduce large-scale seasonal and geographical biases in the retrieved surface salinity fields.

To achieve the 0.1-psu accuracy goal for the retrieved salinity, the sky glitter contribution must be estimated with an uncertainty not exceeding 0.05 K. This is a stringent constraint that may be difficult to satisfy given the accuracies of both the future SMOS radiometric measurements and the sky brightness

Manuscript received March 1, 2007; revised June 20, 2007.

N. Reul, J. Tenerelli, and B. Chapron are with the Laboratoire d'Océanographie Spatiale, Institut Français de Recherche et d'Exploitation de la Mer, 29280 Brest, France (e-mail: nreul@ifremer.fr).

N. Floury is with the Electromagnetics and Space Environments Division, European Space Research and Technology Centre (ESTEC), European Space Agency, 2200 AG Noordwijk, The Netherlands.

Color versions of one or more of the figures in this paper are available online at <http://ieeexplore.ieee.org>.

Digital Object Identifier 10.1109/TGRS.2007.914804

88 temperature maps. This constraint also presents potential dif-
89 ficulties for the forward modeling of the scene brightness
90 temperatures since this modeling is plagued by uncertainties
91 and potential biases associated with rough sea surface scattering
92 and emissivity models. Moreover, for the SMOS mission, the
93 multidirectional nature of the measurements incorporated into
94 the salinity retrieval at any given point on Earth results in a
95 potentially wide range of celestial noise contamination for any
96 given retrieval, so that failure to correct for the contamination
97 prior to salinity retrieval may result in retrieved salinity errors
98 and biases that are not easily correctable by further processing
99 at a later stage.

100 The focus of this paper is given as follows: 1) to analyze the
101 expected annual cycle of contamination of SMOS multiangular
102 reconstructed brightness temperatures by scattered celestial
103 radiation over the ocean and 2) to propose a method for the
104 proper detection of and correct for this sky glitter within the
105 SMOS ocean surface salinity retrieval algorithm.

106 For these two purposes, a sky brightness temperature map
107 at L-band was generated for SMOS based on an existing all-
108 sky continuum map using an approach similar to [2], and the
109 method used to build this map is reviewed in Section II. Missing
110 data in the vicinity of Cassiopeia A and other strong sources in
111 the continuum map can potentially lead to underestimation of
112 the reflected sky noise, particularly over smooth sea surfaces,
113 and to address this issue, we derived an error map by using
114 higher resolution surveys to identify the locations and bright-
115 ness temperatures of sources that may introduce substantial
116 errors associated with estimating the downwelling celestial
117 radiation from the continuum map alone. Since these localized
118 strong sources might require the use of very high-resolution
119 grids when applying the modeling methodology developed in
120 Part I, we evaluated the impact of resolution on the numerical
121 scattering calculations and determined an acceptable discretiza-
122 tion of the celestial noise map.

123 In Section III, we formulate expressions for the rough surface
124 scattered celestial radiation incident at the SMOS antenna. The
125 interferometric nature of the Microwave Imaging Radiometer
126 by Aperture Synthesis (MIRAS) results in a formulation that is
127 distinct from that for a real aperture radiometer. In developing
128 these expressions, we consider, in turn, simplifications that are
129 obtained by assuming that the sea surface is perfectly smooth
130 and approximating the synthetic antenna weighting function by
131 an isotropic function in director cosine (DC) coordinates.

132 Given the potential for scattered celestial noise to introduce
133 seasonal and regional biases in retrieved surface salinity, we ex-
134 amined the seasonality and spatial distribution of the expected
135 celestial sky glitter contamination for SMOS by performing
136 a series of monthly orbit propagations in which we collected
137 dwell lines, i.e., sets of multiangular scene brightness temper-
138 atures at a fixed location on Earth, over a fixed Earth grid
139 that spans one complete orbit. The scattered celestial radiation
140 was calculated for one orbit per month over a one-year period
141 using idealized descriptions of the ocean surface state. Results
142 of these calculations are presented in Section IV. The SMOS
143 configuration, with its sun-synchronous orbit and large field
144 of view (FOV), provides reconstructed brightness temperatures
145 over a large range of incidence and azimuth angles (and there-

fore a large range of specular sky locations) at each point on 146
Earth, so that a large portion of the sky will contribute to 147
the contamination at any given time. Moreover, given the sun- 148
synchronous nature of the SMOS orbit, the celestial sky glitter 149
contamination is a function of time with a distinct annual cycle. 150
This is distinct from the situation with the Aquarius/SAC-D 151
mission, for which the set of all specular sky locations (or 152
specular projection of the FOV) at any given time of year is 153
a large closed loop on the celestial sphere. For SMOS, the 154
error associated with assuming a perfectly smooth sea surface 155
may exceed 0.1 K over large portions of the measurements 156
in an orbit. Both the contamination and the potential error 157
associated with assuming a perfectly flat surface are greatest 158
for the descending passes from August to October. 159

Given the potential for significant impact of the rough ocean 160
surface and the large computational burden associated with the 161
scattering calculations, in Section V, we propose a practical 162
correction and flagging strategy that may be used in a salinity 163
retrieval algorithm. In Section VI, we summarize the results and 164
briefly discuss potential sources of error as well as validation 165
issues for the proposed celestial sky glitter correction. 166

II. GENERATION OF AN L-BAND SKY MAP TO BE 167 USED FOR SMOS DATA PROCESSING 168

Three components are required to build a map of the sky 169
emission at L-band [2]. 170

- 1) The cosmic microwave background (approximately a 171
constant value of 2.725 K). 172
- 2) The neutral hydrogen line (HI in astronomer's shorthand): 173
this strong emitting line is centered at 1420.4058 MHz 174
and is spread over a finite band by an additional Doppler 175
shift. In surveys of the continuum, this source is usually 176
rejected by a stopband filter. 177
- 3) The continuum at ~ 1.4 GHz, which originates from a 178
variety of emission mechanisms (other lines than HI, syn- 179
chrotron, free-free, thermal, blended emission of discrete 180
radio sources, . . .). 181

The final merged map to be used with SMOS, which is 182
termed here as the "nominal map," is expressed in the Besselian 183
Epoch B1950 [4], and in what follows, we display the results 184
(and perform the scattering calculations) in an equatorial coor- 185
dinate system (with coordinates given by right ascension and 186
declination) in this reference frame. 187

A. Main Sources of Data 188

To provide coverage of the whole sky, measurements ob- 189
tained by different instruments situated in both the Northern 190
and Southern Hemispheres must be combined. This requires 191
extensive data collection and calibration to ensure sufficient 192
data quality. The merging of these data sets requires cross cali- 193
bration and consideration for differences in instrument angular 194
resolutions. This work was conducted by experts in the field of 195
radio astronomy, and the maps introduced here are based upon 196
products produced by these experts. 197

1) *Continuum*: The data set identified here is a combination 198
of the Northern Sky survey made with the Stockert radio 199

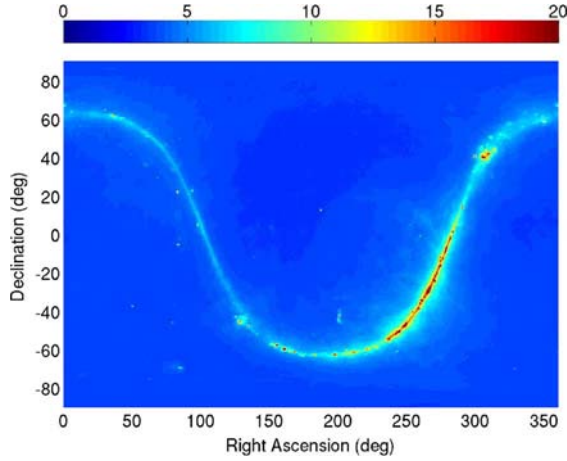


Fig. 1. Reich and Testori continuum map. Dark blue is for 0 K, and red is for 20 K.

200 telescope [5]–[7] and the Southern Sky survey made with the
 201 radio telescope of the Instituto Argentino de Radioastronomia
 202 (IAR) [8]. When the bandwidth of the receiver was overlapping
 203 the HI emission, a stopband filter centered over the HI line
 204 and 2 MHz wide was applied to the measurement to reject it.
 205 Data were sampled with a 0.25° resolution in both declination
 206 and right ascension (equatorial coordinates, B1950 system).
 207 The sensitivity (defined as three times the root-mean-square
 208 brightness temperature noise) of the merged data set is 0.05 K.
 209 In the following, this data set will be referred to as the Reich
 210 and Testori map (Fig. 1).

211 It is assumed that the “continuum” radiation, with unpolar-
 212 ized brightness temperature T_{cont} , is broadband and therefore
 213 does not vary appreciably within the SMOS band. Thus, data
 214 from surveys made at slightly different center frequencies and
 215 with slightly different bandwidths may be directly combined.
 216 The continuum data set includes the constant 2.725 K cosmic
 217 background radiation.

218 2) *Hydrogen Line*: To account for the hydrogen line emis-
 219 sion, we used the Leiden–Argentina–Bonn (LAB) survey [9].
 220 The LAB survey contains the final data release of obser-
 221 vations of 21-cm emission from galactic neutral hydrogen
 222 over the entire sky and is a merged product based on the
 223 Leiden–Dwingeloo survey of the sky north of -30° [10] and
 224 the IAR survey of the sky south of -25° [11], [12]. The
 225 source velocities away from the Earth range from -450 to
 226 $+400 \text{ km} \cdot \text{s}^{-1}$ and are resolved in the data to $1.3 \text{ km} \cdot \text{s}^{-1}$.
 227 The root-mean-square error of the brightness temperatures in
 228 the merged data set is 0.07 – 0.09 K (for each $1.3 \text{ km} \cdot \text{s}^{-1}$ layer).
 229 Data were sampled with a 0.5° resolution in both latitude and
 230 longitude (in galactic coordinates). Hereinafter, this data set
 231 will be referred to as the HI map.

232 3) *Integration of HI Into the Continuum Map*: As men-
 233 tioned earlier, the continuum signal is broadband, with almost
 234 constant brightness temperature T_{cont} throughout the SMOS
 235 bandwidth. By contrast, the hydrogen line emission exists only
 236 over a very narrow band, but MIRAS measures radiation over
 237 a bandwidth B_{SMOS} of 19 MHz that includes the HI line
 238 (1420.4058 MHz) so that this narrow source must be integrated
 239 into the continuum map. The merged all-sky map provided by

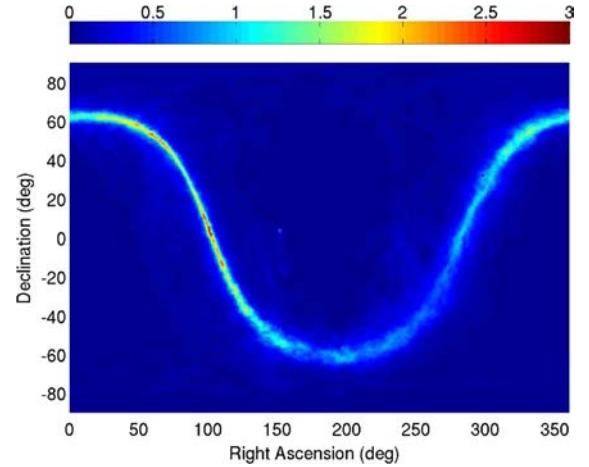


Fig. 2. HI map rescaled over SMOS bandwidth. Dark blue is for 0 K, and red is for 3 K.

Reich and Testori includes both T_{cont} and the constant 2.725 K
 240 cosmic microwave background T_{CMB} . The HI data [9] do not
 241 include T_{CMB} (Fig. 2). 242

243 To derive the HI line contribution over the SMOS bandwidth
 244 from HI line velocity range data, we used a Doppler relation
 245 between velocity range and frequency shift. The HI line fre-
 246 quency is $f_0 = 1420.4058 \text{ MHz}$, and the Doppler shift is given
 247 by $f = f_0(c/(c + \nu))$, where c is the speed of light and ν is the
 248 relative speed of the source away from the Earth. The stopband
 249 filter applied to the Reich and Reich measurements is centered
 250 on f_0 and is $B_{\text{HI}} = 2 \text{ MHz}$ wide. This corresponds to outward
 251 velocities ranging from -211.2 to $+211.4 \text{ km} \cdot \text{s}^{-1}$. Over this
 252 bandwidth, the contribution of HI signal is 252

$$\tilde{T}_{\text{HI}} = \frac{1}{422.6 \text{ km} \cdot \text{s}^{-1}} \int_{-211.2 \text{ km} \cdot \text{s}^{-1}}^{211.4 \text{ km} \cdot \text{s}^{-1}} T_{\text{HI}}(\nu) d\nu. \quad (1)$$

Finally, the resulting sky noise to be considered for SMOS is 253

$$T_{\text{sky}} = T_{\text{CMB}} + T_{\text{cont}} + \tilde{T}_{\text{HI}} \frac{B_{\text{HI}}}{B_{\text{SMOS}}}. \quad (2)$$

B. Gaps in the Continuum Survey: Use of Alternative Surveys and Source Catalogs for Missing Data Integration 254 255

256 The Reich and Testori continuum survey is not complete and
 257 contains regions with inadequate coverage. The most prominent
 258 such region is Cassiopeia A, where the high flux prevented
 259 accurate measurement using standard procedures. In addition,
 260 highly localized strong sources are not properly taken into
 261 account in the continuum survey. Higher resolution surveys that
 262 can alleviate this problem by providing auxiliary 1.4-GHz flux
 263 measurements for these problematic areas are available. These
 264 data sets usually come in two forms. 264

- 1) Higher resolution local sky maps where for a given
 265 area of the sky a radio flux is associated to each [right
 266 ascension, declination] cell. This enables an assessment
 267 of the slow variations of the background flux when it
 268

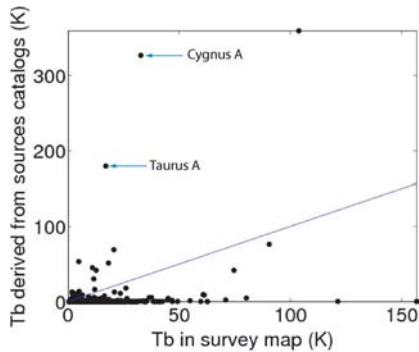


Fig. 3. Comparison between brightness temperatures derived from the individual source catalogs (NVSS + Parkes) and brightness temperatures extracted from the survey maps (i.e., a combination of the merged data from Reich and Testori, the rescaled HI line data from the survey in [9], and the Effelsberg survey data in the vicinity of Cassiopeia A). The diagonal line shows one-to-one correspondence.

269 results from the combination of minor sources that cannot
 270 be individually identified. Once rescaled and converted to
 271 the proper geometry, these data sets can be used to patch
 272 the continuum map where data are missing.

273 2) Source catalogs that provide flux measurements for spe-
 274 cific strong sources with small angular extents. These data
 275 sets can be useful to identify strong sources in otherwise
 276 quiet areas of the sky.

277 In the case of strong sources of small angular extent, it is diffi-
 278 cult to determine whether they are properly taken into account
 279 in the full sky survey map. To evaluate the extent to which
 280 strong sources are properly accounted for in the continuum
 281 map, a map of strong sources was generated from L-band
 282 source catalogs [13], [14], and we computed the corresponding
 283 brightness temperatures that would be collected by the Stockert/
 284 IAR radio telescopes (the ones that were used to generate the
 285 Reich and Testori map). These source data were obtained from
 286 both the [NRAO (National Radio Astronomy Observatory)
 287 VLA (Very Large Array) Sky Survey (NVSS)] [14] (Northern
 288 Hemisphere) and the Parkes [13] (Southern Hemisphere) cata-
 289 logs. Only sources stronger than 0.3 Jy were considered, since
 290 smaller fluxes would introduce less than 0.015-K error in the
 291 Reich and Testori map.

292 The resulting brightness temperatures were compared with
 293 the combination of the continuum and HI maps. Fig. 3 shows
 294 that most sources exhibit a brightness temperature that does
 295 not exceed the corresponding continuum value (which is gen-
 296 erally the case when the sources are embedded in regions of
 297 strong emission that dominate the total signal within the rela-
 298 tively large beam of the telescope). Nevertheless, some strong
 299 sources, such as Cygnus A and Taurus A, can be identified.
 300 Fig. 4 shows the locations of the sources for which the fluxes
 301 are undervalued in the nominal sky map. Most discrepancies
 302 in the flux are quite small and are expected to be strongly
 303 reduced when integrated over the SMOS synthetic beam. The
 304 strongest discrepancies occur in the vicinity of Cygnus A and
 305 Cassiopeia A. The nominal sky map generated for SMOS was
 306 not corrected for these strong sources; instead, a separate sky
 307 map that contains only the strong source brightness temper-
 308 atures averaged to the Stockert/Testori beamwidth was devel-

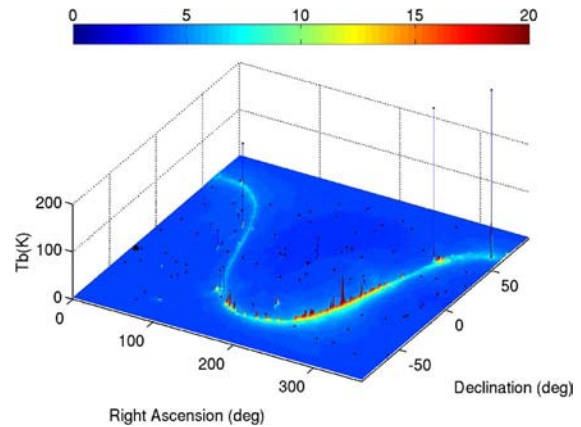


Fig. 4. Strong sources superimposed on the nominal SMOS sky map derived from the survey data of Reich and Testori, the rescaled HI line data from the survey in [9], and the Effelsberg survey data in the vicinity of Cassiopeia A. Only sources that exhibit a brightness temperature (for a 35-arcmin beam) larger than that in the nominal sky map are displayed.

oped. As in [2], we do not account for possible polarization in
 either the nominal or the strong source maps. 310

C. Impact of Strong Sources 311

To quantify the maximum expected impact of strong point
 sources, we calculated the scattered signal along cross sections
 through Cassiopeia A, where the strongest sources are located,
 at both full ($0.25^\circ \times 0.25^\circ$) and reduced-resolution ($3.75^\circ \times 3.75^\circ$)
 celestial grid spacings for both the nominal and strong source
 maps. The reduced-resolution map was obtained by applying an
 energy flux-conserving averaging operator, which is described in
 the Appendix, to the full-resolution map. The results are shown
 in Fig. 5. To provide an indication of the spatial extent of the
 bistatic scattering cross sections on the celestial map, in Fig. 5(a),
 we overlay on the total celestial noise map (centered on Cassiopeia
 A) the weighting function associated with the scattering cross sections
 for a representative scattering calculation at a wind speed of
 $7 \text{ m} \cdot \text{s}^{-1}$. The total scattered signal in the direction of the
 instrument is obtained by integrating the product of this weight-
 ing function and the sky brightness temperatures over the sky
 map. The downwind direction φ_w relative to the scattering azimuth
 ϕ_s (both defined to be positive counterclockwise from due east)
 is $\varphi_w - \phi_s = 0^\circ$. This weighting function has been normalized to
 a maximum of unity, and contours are shown at 0.1, 0.3, 0.5, 0.7,
 and 0.9. Clearly, the weighting function extends well beyond the
 localized strong source, so it is expected that the impact of such
 a source should be small. In Fig. 5(b), we show the scattered
 unpolarized signal ($1/2(T_v + T_h)$) along a cross section at
 constant declination in the celestial sphere, considering only the
 strong source map. In this cross section, the wind speed is fixed
 at $7 \text{ m} \cdot \text{s}^{-1}$, the specular declination is 58.25° , the scattered
 field incidence angle is 0° , and the specular right ascension
 ranges from -40° to $+20^\circ$. The resulting glitter is shown for
 both the Kirchhoff approximation (KA) [15] and the first-order
 small slope approximation (SSA-1) [16] scattering models
 described in [3] and for both the full-resolution and reduced-
 resolution maps. The resulting glitter never exceeds

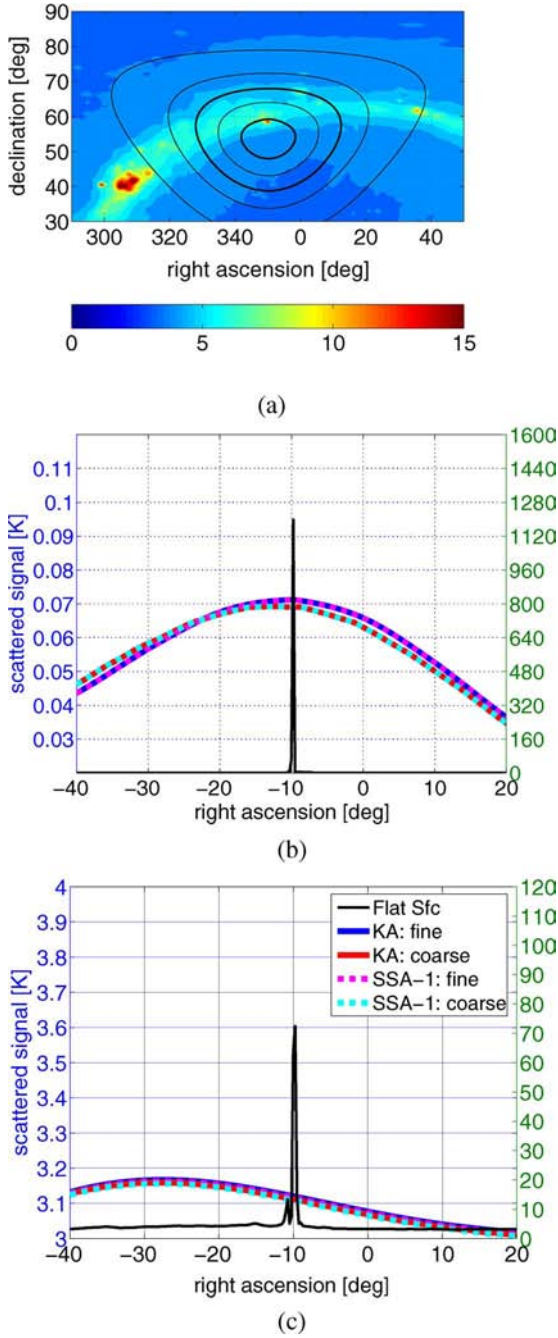


Fig. 5. (a) Incident unpolarized celestial noise. Overlaid is the bistatic scattering weighting function (discussed further in the text) for horizontal polarization for a specular point defined by $(\alpha_s = 350.25^\circ, \delta_s = 58.5^\circ)$ (Kirchhoff model; Kudryavtsev wave spectrum), which is normalized to unit amplitude. Thin contour lines correspond to the normalized levels (0.1, 0.3, 0.7), and thick contour lines correspond to the normalized levels (0.5, 0.9). (b) Cross section, at constant declination, of the unpolarized $(1/2(T_v + T_h))$ scattered radiation from strong sources as determined using the KA [15] and SSA-1 [16] electromagnetic models and the Kudryavtsev equilibrium ocean surface wave spectrum. Curves are defined in the inset of (c). The specularly reflected signal (solid black curve) is scaled to the right axis, whereas the scattered signals are scaled to the left axis. (c) Same as in (b) except for the nominal celestial noise map without strong sources. The scattered signal is evaluated at an incidence angle of $\theta_s = 0^\circ$ and the incidence plane orientation angle $\psi_{uh} = 0^\circ$. The surface wind speed is $u_{10} = 7 \text{ m} \cdot \text{s}^{-1}$; the downwind direction relative to the scattering azimuth is $\varphi_w - \phi_s = 0^\circ$. The maximum incident signal in the strong source map exceeds 1700 K, while in the nominal map the maximum signal in the vicinity of this strong source is approximately 150 K [with a maximum at a slightly displaced position of $(\alpha_s = 350.25^\circ, \delta_s = 58.25^\circ)$]. Units are in kelvin.

about 0.07 K, and the differences between solutions based on 346 the two scattering models and two map resolutions are negligi- 347 ble, even for this source with a peak brightness temperature ex- 348 ceeding 1100 K. 349

Results from the same calculation with the nominal map are 350 shown in Fig. 5(c), where it is seen that differences between 351 resolutions and models are negligible, just as with the strong 352 source map. Notably, the maximum in the glitter does not 353 coincide with the strongest source, which can be understood 354 by examination of Fig. 5(a), which shows that the maximum 355 scattered signal can be expected when the overlap between the 356 weighting function and the galactic equator reaches a max- 357 imum. This maximum occurs for a specular point displaced 358 significantly from Cassiopeia A toward smaller right ascension. 359

III. CELESTIAL SKY GLITTER CONTRIBUTION 360 AT THE SMOS INSTRUMENT LEVEL 361

In Part I, we examined the rough surface scattered noise with- 362 out reference to a specific observational platform. Although the 363 results of that study provide an indication of expected depen- 364 dence of the scattered celestial sky glitter on both geophysical 365 variables (such as wind speed and direction) and observational 366 geometry, they do not address the impact of antenna patterns 367 and the potential systematic contamination associated with 368 orbit and viewing geometry. In this section, we consider the 369 impact of the SMOS synthetic antenna weighting function on 370 the resulting contamination. 371

A. General Formulation 372

Considering the simple case of unpolarized celestial radia- 373 tion with scalar brightness temperature T_{sky} and assuming a 374 simple exponential model for attenuation on both downward 375 and upward paths, it was shown in Part I that the total antenna 376 temperature Stokes component p (where p corresponds to either 377 horizontal or vertical polarization) associated with rough sea 378 scattered celestial radiation is 379

$$\begin{aligned} \bar{\mathbf{T}}_p^a = & \frac{1}{\Omega_a} \int_{\Omega_a} \frac{(\mathbf{GM}_\alpha)}{4\pi \cos \theta_s} e^{-a \sec \theta_s} \\ & \times \int_{\Omega_0(\Omega_a)} [\sigma_{pp}(\Omega_0) + \sigma_{pq}(\Omega_0)] e^{-a \sec \theta_0} T_{\text{sky}}(\Omega_0) d\Omega_0 d\Omega_a \end{aligned} \quad (3)$$

where the factor in front of the outermost integral normalizes 380 the antenna gain pattern \mathbf{G} . As detailed in Part I, \mathbf{M}_α is a 381 composite transformation matrix accounting for polarization 382 basis and Faraday rotation. The scattered field incidence angle 383 is θ_s , and σ_{pq} are the normalized bistatic scattering cross 384 sections of the rough sea surface defined using the forward 385 scattering alignment polarization basis convention as discussed 386 in Part I and in [17]; Ω_a refers to the solid angle domain 387 of integration over the antenna pattern and is associated with 388 antenna incident and azimuth angles θ_a and ϕ_a , respectively; 389 Ω_0 refers to the entire upper hemisphere of over which sky 390 radiation is incident at the target; a is the zenith atmospheric 391

392 attenuation. Note that the normalized bistatic scattering cross
393 sections used in this paper and in Part I differ from the bistatic
394 scattering coefficients γ_{pq} used in [1] in that the normalized
395 scattering cross sections relate scattered wave energy flux
396 across the undisturbed scattering surface to the incident flux
397 in the incident wave propagation direction, whereas the bistatic
398 scattering coefficients relate the scattered energy flux across the
399 surface to the incident energy flux across the surface, so that
400 $\sigma_{pq} = \cos \theta_0 \gamma_{pq}$. This distinction is briefly discussed in [18].

401 In the case of an interferometric instrument such as MIRAS,
402 we are concerned with modeling the reconstructed brightness
403 temperature rather than the conventional antenna temperature
404 as obtained from a real aperture radiometer. The reconstructed
405 brightness temperature in direction (θ_a, ϕ_a) is still given by an
406 equation of the form (3), but the outermost integral over Ω_a
407 is evaluated over a rather narrow synthetic antenna weighting
408 function centered at synthetic boresight direction (θ_a, ϕ_a) , and
409 the real aperture antenna gain matrix \mathbf{G} is replaced by a
410 synthetic antenna weighting function that, in general, depends
411 upon both the instrument and the image reconstruction method.
412 In what follows, we will use the terms “reconstructed brightness
413 temperatures” and “brightness temperature measurements” in-
414 terchangeably.

415 If we introduce instrument DC coordinates (ξ, η)

$$\xi = \sin \theta_a \cos \phi_a \quad (4)$$

$$\eta = \sin \theta_a \sin \phi_a \quad (5)$$

416 then the SMOS synthetic antenna weighting function, which is
417 also called equivalent array factor (AF), may be written [19] as

$$\begin{aligned} \text{AF}_{\text{eq}}(\xi, \xi', \eta, \eta') &= \frac{\sqrt{3}}{2} d^2 \sum_m \sum_n W(u_{mn}, v_{mn}) \\ &\times \tilde{r} \left(-\frac{u_{mn} \cdot \xi + v_{mn} \cdot \eta}{f_0} \right) \\ &\times e^{j2\pi(u_{mn} \cdot (\xi - \xi') + v_{mn} \cdot (\eta - \eta'))} \quad (6) \end{aligned}$$

418 where W is the apodization function; \tilde{r} is the fringe-washing
419 factor (FWF), which accounts for the spatial decorrelation
420 between antennas; u, v are the baseline coordinates in the
421 frequency domain; d is the dimensionless antenna element
422 spacing (0.875); f_0 is the central frequency (1413 MHz); ξ, η
423 are the central (i.e., synthetic boresight) DC coordinates; and
424 ξ', η' are the running DC coordinates. Defining $\mathcal{D} = \{\xi', \eta' : 425 \xi'^2 + \eta'^2 < 1\}$ as the domain of integration within the synthetic
426 beam and noting that

$$d\Omega_a = \sin \theta_a d\theta_a d\phi_a = \frac{d\xi d\eta}{\cos \theta_a} = \frac{d\xi d\eta}{\sqrt{1 - \xi^2 - \eta^2}} \quad (7)$$

427 the expression for the contribution of the polarized celestial
428 sky glitter to the reconstructed brightness temperature in the
429 Ludwig-3 polarization basis is given by

$$\begin{aligned} \bar{\mathbf{T}}_p^a(\xi, \eta) &= \iint_{\mathcal{D}} \frac{\text{AF}_{\text{eq}}(\xi, \xi', \eta, \eta')}{\sqrt{1 - (\xi' - \xi)^2 - (\eta' - \eta)^2}} \\ &\times [\mathbf{M}_\alpha(\xi', \eta') \mathbf{A}_u(\xi', \eta')] \tilde{\mathbf{T}}_p^a(\xi, \xi', \eta, \eta') d\xi' d\eta' \quad (8) \end{aligned}$$

where $\tilde{\mathbf{T}}_p^a(\xi, \xi', \eta, \eta')$ is the Stokes vector of the surface scat- 430
tered celestial noise in the target polarization basis, and \mathbf{A}_u 431
is an upward atmospheric attenuation matrix defined in Part I. 432
The variations in atmospheric attenuation and geometrical rota- 433
tion are sufficiently small within the narrow (approximately 3°) 434
synthetic beam that these factors may be approximated by their 435
values at the synthetic beam center, i.e., (ξ, η) , so that 436

$$\begin{aligned} \bar{\mathbf{T}}_p^a(\xi, \eta) &\simeq \mathbf{M}_\alpha(\xi, \eta) \mathbf{A}_u(\xi, \eta) \\ &\times \iint_{\mathcal{D}} \frac{\text{AF}_{\text{eq}}(\xi, \xi', \eta, \eta')}{\sqrt{1 - (\xi' - \xi)^2 - (\eta' - \eta)^2}} \tilde{\mathbf{T}}_p^a(\xi, \xi', \eta, \eta') d\xi' d\eta'. \quad (9) \end{aligned}$$

As shown in [20], if one neglects the FWF, the AF may be 437
approximated by a rather narrow centrosymmetric function 438
that is independent of the location of the synthetic boresight 439
 (ξ, η) within the FOV. The following explicit formula has been 440
developed to approximate the actual AF with no FWF effect: 441

$$\begin{aligned} \text{AF}_{\text{eq}}(\xi, \xi', \eta, \eta') &\simeq F_{\text{cs}}(\rho(\xi, \xi', \eta, \eta')) \\ &= \max \left\{ 0, \left[\frac{\sin k_f \cdot \rho}{k_f \cdot \rho} \right]^{k_k} \cdot \frac{1}{1 + k_g \cdot \rho^{k_h}} \right\} \quad (10) \end{aligned}$$

where $\rho = \sqrt{(\xi' - \xi)^2 + (\eta' - \eta)^2}$ is the distance in DC co- 442
ordinates, $k_f = 73.30$, $k_g = 524.5$, $k_h = 2.1030$, and $k_k = 443$
1.4936. Throughout the rest of this paper, we refer to the 444
approximate AF expression (10) as the antenna weighting 445
function, i.e., WEF. If we adopt this approximate formulation 446
for the AF and assume that the downwelling sky radiation 447
is unpolarized, then the total contamination of reconstructed 448
brightness temperatures by scattered celestial sky glitter (3) 449
becomes 450

$$\begin{aligned} \bar{\mathbf{T}}_p^a(\xi, \eta) &\simeq \frac{\mathbf{M}_\alpha(\xi, \eta)}{4\pi \cos \theta_s(\xi, \eta)} e^{-a \sec \theta_s(\xi, \eta)} \iint_{\mathcal{D}_\rho} d\phi d\rho \frac{\rho F_{\text{cs}}(\rho)}{\sqrt{1 - \rho^2}} \\ &\times \int_{\Omega_0} [\sigma_{pp}(\Omega_0) + \sigma_{pq}(\Omega_0)] e^{-a \sec \theta_0} T_{\text{sky}}(\Omega_0) d\Omega_0. \quad (11) \end{aligned}$$

In this equation, $\mathcal{D}_\rho = \{\rho, \phi : (\xi'(\rho, \phi))^2 + \eta'((\rho, \phi))^2 < 1\}$ is 451
the polar coordinate domain corresponding to the Cartesian 452
domain \mathcal{D} . 453

B. Perfectly Smooth (Flat) Sea Surface Case 454

When the sea surface is perfectly flat, the scattered celestial 455
sky glitter incident at the instrument in the surface polarization 456
basis reduces to 457

$$\tilde{\mathbf{T}}_p^f = \left| R_{pp}^{(0)}(S, T_s, \theta_s) \right|^2 T_{\text{sky}}(\theta_s, \phi_s - \pi) e^{-a \sec \theta_s} \quad (12)$$

where $R_{pp}^{(0)}(S, T_s, \theta_s)$ are the Fresnel reflection coefficients of 458
the flat sea surface with salinity S , physical surface temperature 459
 T_s , incidence angle θ_s , and linear polarization p . In this case, 460

461 the contribution to the reconstructed brightness temperature
462 from the sky glitter incident at the antenna from direction (ξ, η) ,
463 which is expressed in the instrument polarization basis, is

$$\begin{aligned} \bar{T}_p^{fa}(\xi, \eta) &\simeq (\mathbf{M}_\alpha(\xi, \eta) \mathbf{A}_u(\xi, \eta)) \iint_{\mathcal{D}} \frac{\text{AF}_{\text{eq}}(\xi, \xi', \eta, \eta')}{\sqrt{1 - (\xi' - \xi)^2 - (\eta' - \eta)^2}} \\ &\times \left| R_{pp}^{(0)}(S, T_s, \theta_s(\xi', \eta')) \right|^2 \\ &\times T_{\text{sky}}(\xi, \eta, \xi', \eta') e^{-a \sec \theta_0(\xi', \eta')} d\xi' d\eta'. \end{aligned} \quad (13)$$

464 The Fresnel power reflection coefficients vary weakly over the
465 significant portion of the synthetic beam, so that

$$\left| R_{pp}^{(0)}(S, T_s, \theta_s(\xi', \eta')) \right|^2 \simeq \left| R_{pp}^{(0)}(S, T_s, \theta_s(\xi, \eta)) \right|^2. \quad (14)$$

466 With this approximation, the celestial sky glitter contribution at
467 the SMOS antenna for a perfectly flat sea surface becomes

$$\begin{aligned} \bar{T}_p^{fa}(\xi, \eta) &\simeq \mathbf{M}_\alpha(\xi, \eta) e^{-a \sec \theta_s(\xi, \eta)} \left| R_{pp}^{(0)}(S, T_s, \theta_s(\xi, \eta)) \right|^2 \\ &\times \iint_{\mathcal{D}_\rho} \frac{\rho F_{\text{cs}}(\rho)}{\sqrt{1 - \rho^2}} T_{\text{sky}}(\xi, \eta, \rho, \phi) e^{-a \sec \theta_0(\phi, \rho)} d\phi d\rho. \end{aligned} \quad (15)$$

468 If we ignore the downward atmospheric attenuation, then the
469 approximate formulation (15) for a perfectly smooth ocean
470 surface is particularly attractive from a processing point of
471 view because it allows the incorporation of the antenna pattern
472 effect by a presmoothing of the sky brightness temperature map
473 [i.e., the integral factor in (15)] with the idealized synthetic
474 antenna weighting function. The synthetic beam-weighted re-
475 flected celestial sky glitter contamination may then be obtained
476 for arbitrary viewing geometry with a simple interpolation from
477 the smoothed map followed by a matrix multiplication.

478 C. Antenna Pattern Smoothing Versus Roughness Spreading

479 Following (11), to properly account for the celestial glitter in
480 the presence of surface roughness, we must compute the scat-
481 tered noise throughout the synthetic beam and then integrate the
482 product of the weighting function F_{cs} and this scattered signal.
483 Such a computation is not practical, and hence, it is useful to
484 determine if we can avoid this averaging operation. To assess
485 the impact of the synthetic beam averaging, we selected a time
486 and satellite configuration such that a small but strong bright-
487 ness source exists inside the SMOS FOV. We then established
488 a fine mesh over a small portion of the FOV surrounding this
489 source (a 65×65 regular grid covering a 0.2×0.2 domain
490 in the antenna DC coordinates) and calculated the scattered
491 horizontally polarized signal (in the surface polarization basis)
492 at each grid point. The flat surface reflected signal with no
493 synthetic beam smoothing, which is shown in Fig. 6(a), exhibits
494 a maximum brightness temperature of approximately 50 K.
495 The corresponding signal as smoothed by the synthetic beam,
496 which is shown in Fig. 6(b), is significantly smoother, with a
497 maximum brightness temperature of approximately 16 K.

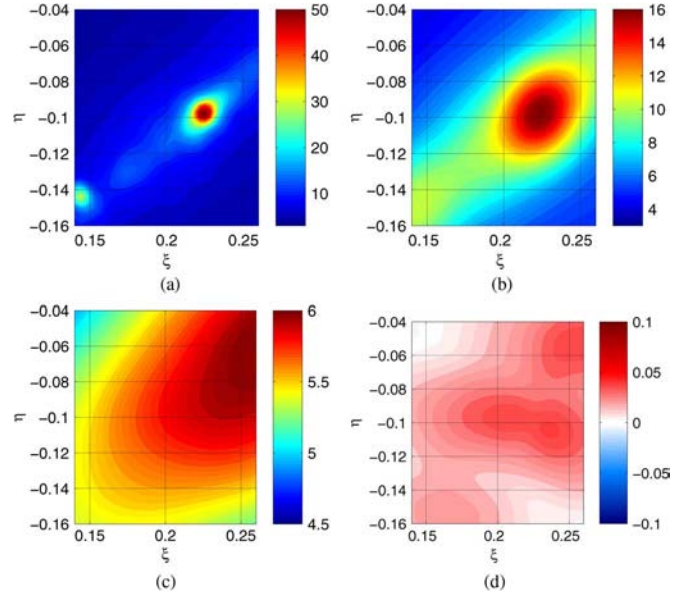


Fig. 6. (a) Flat sea surface specularly reflected signal at horizontal polarization. (b) Flat sea surface specularly reflected signal at horizontal polarization weighted by centrosymmetric WEF. (c) Bistatically scattered signal at horizontal polarization for a wind speed of 3 m/s. (d) Difference between scattered horizontally polarized celestial noise with and without weighting by the WEF. Units are in kelvin.

However, based on the scattering solutions obtained in this
498 paper, the impact of synthetic beam smoothing is far less than
499 that owing to the directional spreading of the radiation by the
500 roughened ocean surface, even at a wind speed of $3 \text{ m} \cdot \text{s}^{-1}$
501 [Fig. 6(c)]. This rough surface smoothing is sufficiently large
502 that applying the WEF smoothing to the scattering solutions
503 yields little change (generally less than about 0.05 K), as shown
504 in Fig. 6(d). We conclude that the application of the WEF is
505 not necessary in the presence of surface roughness, so long as
506 this roughness is uniform within the synthetic antenna beam.
507 Although the WEF impact might be nonnegligible for surface
508 roughness at wind speeds lower than $3 \text{ m} \cdot \text{s}^{-1}$ or for highly
509 heterogeneous rough surfaces, in what follows, we neglect this
510 impact except for perfectly smooth surface conditions. 511

Without the WEF smoothing, the contribution of rough sur-
512 face scattered celestial sky glitter to the reconstructed bright-
513 ness temperatures reduces to 514

$$\begin{aligned} \bar{\mathbf{T}}_p^a(\xi, \eta) &\simeq \frac{\mathbf{M}_\alpha(\xi, \eta)}{4\pi \cos \theta_s(\xi, \eta)} e^{-a \sec \theta_s(\xi, \eta)} \\ &\times \int_{\Omega_0} [\sigma_{pp}(\Omega_0) + \sigma_{pq}(\Omega_0)] e^{-a \sec \theta_0} T_{\text{sky}}(\Omega_0) d\Omega_0 \end{aligned} \quad (16)$$

and this equation is the basis for the results that follow. 515

IV. ANNUAL CYCLE OF CELESTIAL SKY GLITTER CONTAMINATION FOR SMOS 516 517

A. Orbit Propagation and Dwell Line Generation 518

Having established a reasonable approximation for the im-
519 pact of scattered celestial noise on the measurements, we
520 now quantify the impact of celestial sky glitter on SMOS
521

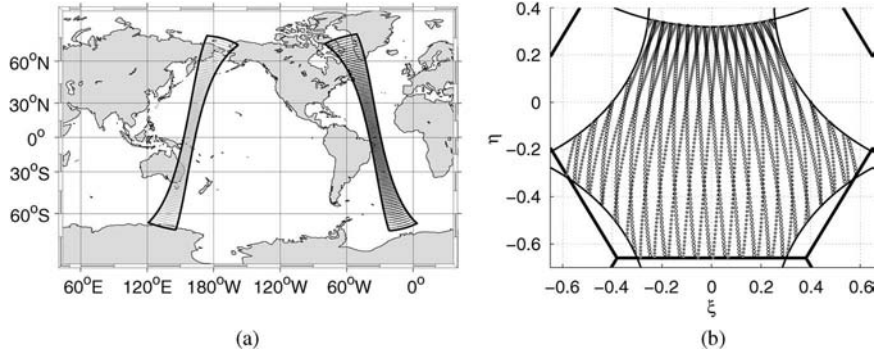


Fig. 7. (a) Fixed points on Earth at which we compute dwell lines for both ascending and descending swaths. (b) Projections of dwell lines in DC coordinates. Circles correspond to an ascending pass, while solid dots correspond to a descending pass.

522 measurements throughout the year. Given the sun-synchronous
 523 nature of the SMOS orbit, the sky noise impact is expected to
 524 exhibit a distinct annual cycle. To examine this annual cycle,
 525 we performed a series of orbit propagations, with successive
 526 orbits spaced roughly one month apart. Although we considered
 527 both idealized and realistic geophysical conditions, here, we
 528 present only the results from the idealized simulations (with
 529 constant roughness conditions) to emphasize the impact of the
 530 viewing geometry on the results. Introducing spatial and tem-
 531 poral variabilities in the surface wind speed complicates the
 532 interpretation of statistics and obscures the results, and the
 533 expected behavior in variable wind conditions may be antici-
 534 pated from the results presented in Part I. For the present sim-
 535 ulations, bistatic scattering cross sections were evaluated at a
 536 constant SSS of 35 psu and temperature of 15 °C. As discussed
 537 in Part I, these two geophysical parameters will have a small
 538 impact on diffuse scattering of celestial sky radiation. For com-
 539 parison purposes, these surface conditions were also used to
 540 estimate the contamination assuming a perfectly smooth ocean
 541 surface. Moreover, to simplify the interpretation, we neglected
 542 downward and upward atmospheric attenuation and only con-
 543 sidered results for the first Stokes parameter (which is not
 544 affected by the Faraday rotation on the upward path across the
 545 ionosphere).

546 Orbit simulations were conducted using the same orbital
 547 and instrument configuration anticipated for the actual satellite.
 548 SMOS will be placed in a circular sun-synchronous low Earth
 549 orbit at a mean flight altitude of 755 km. The local time of
 550 the ascending node will be 6:00 A.M., and the inclination of
 551 the orbital plane will be 98.42°. In addition, the antenna array
 552 plane will be tilted from the horizontal by 32°. To produce
 553 one orbit simulation, we first established a fixed Earth grid by
 554 propagating the satellite through one orbit at a time step of 24 s
 555 and projecting onto the Earth's surface a set of points along a
 556 cross-track line at $\eta = 0.0$ in the instrument frame DC coordi-
 557 nates. As illustrated in Fig. 7(a), this procedure establishes a
 558 21×250 point fixed grid \mathbf{E}_{ij} on the Earth's surface, with
 559 250 rows (with index i) of 21 projected $\eta = 0$ points (with
 560 index j). Having established this grid, we then propagated the
 561 satellite through the same orbit but with a 2.4-s time step,
 562 producing a set of snapshots \mathcal{S}_k . At each of the 21×250 grid
 563 points in a given SMOS FOV, we recorded parameters such
 564 as the incidence and azimuth angles at target and the location

in antenna frame (ξ_s, η_s) . The result is a grid of dwell lines,
 565 where a dwell line at grid point (i, j) , which is denoted as \mathcal{D}_{ij} ,
 566 consists of a set of all k for which \mathcal{S}_k contains the point \mathbf{E}_{ij}
 567 together with the corresponding set of positions in those snap-
 568 shots, i.e.,
 569

$$\mathcal{D}_{ij} = \{k, \xi(i, j, k), \eta(i, j, k) : (\xi(i, j, k), \eta(i, j, k)) \in \mathcal{S}_k\}. \quad (17)$$

Fig. 7(b) shows examples of dwell lines in DC coordinates. 570

In the following experiments, we configured each orbit in the
 571 monthly sequence of orbits so that the grid points do not change
 572 location from one month to the next. Since we only consider
 573 constant geophysical conditions, this has no significance be-
 574 yond the fact that the geographical locations of the grid points
 575 remain the same from one month to the next. 576

B. Perfectly Smooth Sea Surface Contamination 577

Before evaluating the impact of rough surface scattered sky
 578 noise, we establish the impact of flat surface reflected noise as a
 579 baseline. In Fig. 8, we show for each orbit the fraction of mea-
 580 surements contaminated by unpolarized reflected celestial noise
 581 $(1/2(T_v + T_h))$ exceeding 4 K. Most notable is the fact that the
 582 reflected celestial sky noise is quite different for the ascending
 583 and descending swaths, with generally larger contamination
 584 in the descending swaths, which is to be expected since the
 585 specular points for dwell lines on the descending swaths tend
 586 to be aligned with the strongest portion of the noise originating
 587 near the galactic equator. The contamination is greatest during
 588 the northern hemisphere autumn when the specular points
 589 tend to be nearest the galactic equator. A significant portion
 590 of the dwell lines for the September 28 descending swath
 591 have nearly 90% of their reconstructed brightness temperatures
 592 contaminated by flat surface reflected noise exceeding 4 K. 593
 The viewing geometry along any given dwell line is such that
 594 the contamination patterns tend to be elongated in the FOV. 595
 There is no time of the year that the entire swath is severely
 596 contaminated. However, during certain times of the year, the
 597 fraction of measurements suffering significant contamination
 598 may be large. The contamination is also a function of latitude,
 599 and the descending swaths in September tend to suffer from
 600 more contamination in the Northern Hemisphere than in the 601

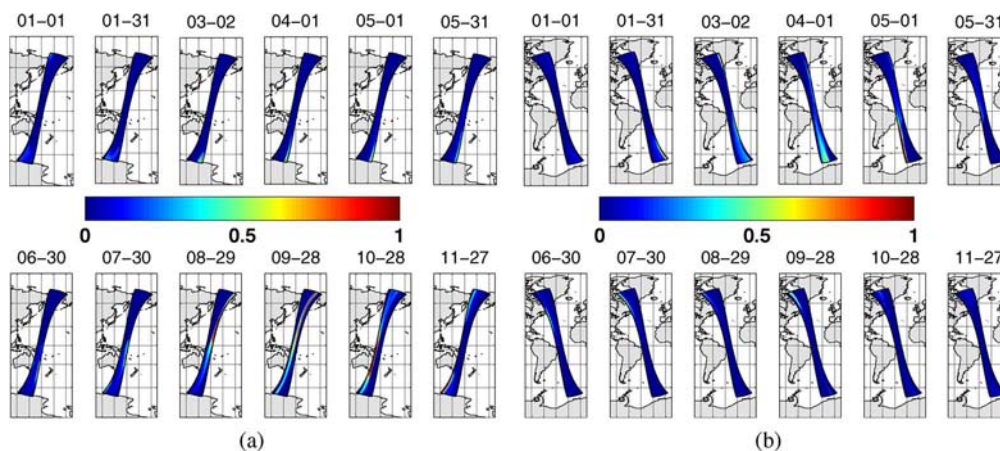


Fig. 8. Fraction of dwell line brightness temperature measurements contaminated by perfectly smooth sea surface reflected celestial noise ($1/2(T_v + T_h)$) greater than 4 K, for each month of the year. (a) Descending swaths. (b) Ascending swaths. The orbit dates (month-day) are indicated above each swath.

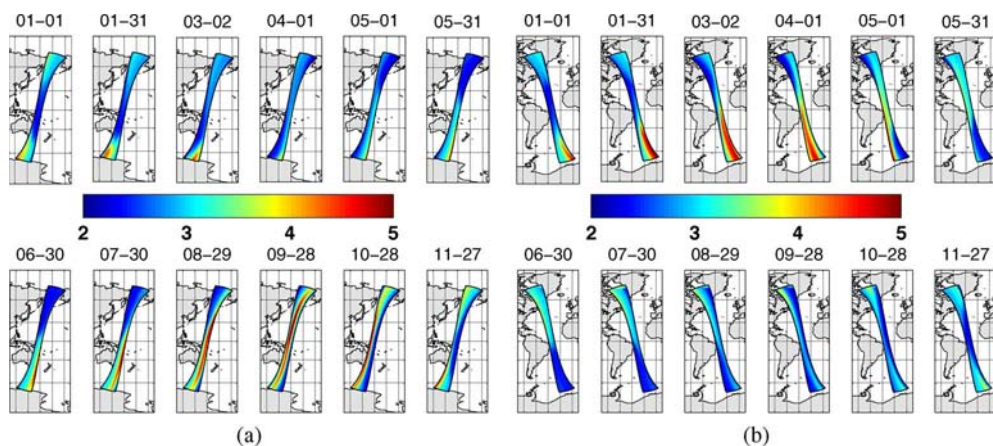


Fig. 9. Maximum unpolarized scattered celestial noise ($1/2(T_v + T_h)$) over all measurements of each dwell line for (a) descending and (b) ascending swaths. The wind speed is $7 \text{ m} \cdot \text{s}^{-1}$, and the downwind direction is 0° . The Kudryavtsev wave spectrum and the KA scattering model are used to compute the scattered signal. Solutions are expressed in kelvin.

602 Southern Hemisphere. In October, the contamination maximum
603 shifts to the Southern Hemisphere.

604 C. Rough Surface Contamination

605 Although examination of the flat surface reflected cele-
606stial noise provides some indication of expected contamination
607 patterns, it does not provide a realistic picture of the true
608 magnitude of the contamination, since at any given time only
609 about 5% of the Earth's ocean surface is nearly perfectly
610 smooth [21]. As discussed in Part I, the differences between
611 the smooth surface reflected and rough surface scattered sig-
612nals may be large, even at wind speeds below $7 \text{ m} \cdot \text{s}^{-1}$. In
613 this section, we examine the expected contamination pattern
614 for SMOS in idealized rough sea surface conditions with a
615 constant wind speed of $7 \text{ m} \cdot \text{s}^{-1}$ and downwind direction of
616 0° . Using the Kudryavtsev equilibrium wave spectrum [22] and
617 the Kirchhoff scattering model (see Part I), we computed the
618 expected rough surface scattered celestial noise over the same
619 dwell lines considered in the previous section. In Fig. 9, we
620 show the maximum predicted unpolarized scattered sky noise
621 ($1/2(T_v + T_h)$) for both descending and ascending passes
622 throughout the year. Both the spatial and temporal structures

of the contamination are similar to those of the flat surface
623 contamination, but in the rough surface case, the patterns tend to
624 be smoother with significantly lower maximum contamination,
625 as one would expect from the results presented in Part I. 626
627 The strong maximum contamination first appears in late June
628 in the southern hemisphere and propagates across the FOV
629 toward higher ξ in DC coordinates as time progresses. By
630 September 28, the peak contamination is situated near the
631 middle of the swath and nearly extends from pole to pole on
632 Earth. By late November, this maximum has shifted off the
633 right-hand side of the FOV.

In the ascending swaths, the time of year of maximum
634 contamination is different. The peak contamination, which is
635 slightly smaller in magnitude (approximately 4.7 K) than for the
636 descending swaths, begins to enter the swath in early January
637 and propagates toward the west and north within the swath,
638 reaching the domain center in March, when it extends from the
639 South Pole to near the Earth's equator. By the end of May, the
640 peak has nearly left the swath.

The results for all of the orbits show that the time periods
642 of maximum contamination for the ascending and descending
643 swaths are nearly disjoint. At any given time of the year, either
644 the ascending or descending swaths, but not both, will suffer
645

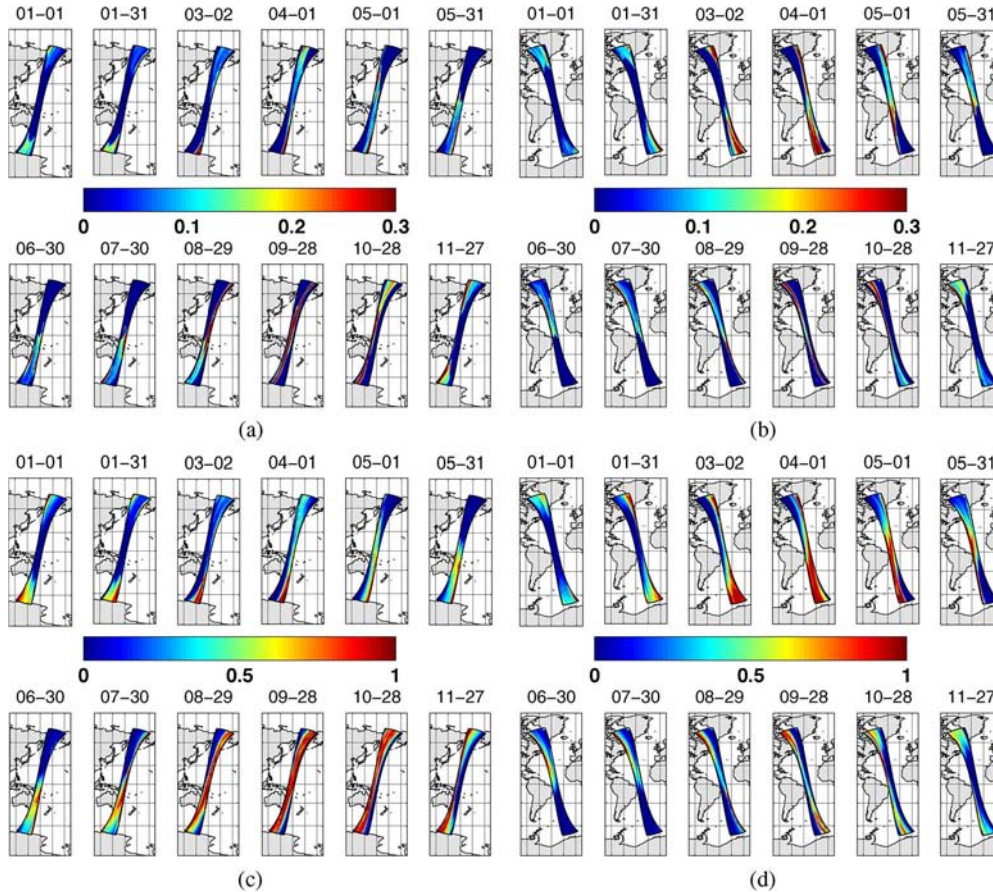


Fig. 10. (a) and (b) Fraction of dwell line brightness temperature measurements for which the difference between the unpolarized flat surface reflected signal ($1/2(T_v + T_h)$) differs from the bistatically scattered signal by more than 0.5 K, for descending and ascending swaths, respectively; (c) and (d): Same as in (a) and (b) except that the cutoff difference is 0.1 K. The geophysical conditions are the same as in Fig. 9.

646 contamination. Given the relative ease with which contamina-
 647 tion of reconstructed brightness temperatures by flat surface
 648 reflected celestial noise may be evaluated, it is important to
 649 determine if a more involved computation of the rough surface
 650 scattered celestial noise will yield significantly different results.
 651 Therefore, we assessed the overall difference between results
 652 based on flat surface reflection and those based on rough surface
 653 scattering calculations. Fig. 10(a) shows, at each dwell line of
 654 the descending swaths, the fraction of measurements for which
 655 the absolute difference between the perfectly smooth and rough
 656 surface solutions exceeds 0.5 K. The maxima in this fraction
 657 generally exceed 10% and tend to coincide with the maxima in
 658 the contamination. Similar results were obtained for the ascend-
 659 ing swaths [Fig. 10(b)]. The fraction of measurements for which
 660 the difference between the flat and rough solutions exceeds
 661 0.1 K approaches 100% for a substantial number of dwell lines,
 662 as shown in Fig. 10(c) and (d). Given that the maxima in the
 663 difference between the flat and rough surface solutions tend to
 664 coincide with the maxima in the flat surface reflected noise, one
 665 might hope to be able to develop a correction and error flagging
 666 strategy based upon the flat surface solution. Unfortunately, the
 667 differences between the flat and rough surface solutions do not
 668 exactly coincide with the flat surface solution because the rough
 669 surface scattering solutions depend strongly upon the spatial
 670 structure of the source in the vicinity of the specular direction;

therefore, it is not possible to determine a universal threshold
 based on the flat surface solution alone.

V. PROCESSING ISSUES

Given the significant and systematic impact of ocean surface
 roughness on the contamination of reconstructed brightness
 temperatures by celestial sky glitter, it is certainly desirable to
 have a practical correction and flagging strategy for operation
 purposes that incorporates the effect of surface roughness. Un-
 fortunately, it is not practical to perform per-measurement inte-
 grations of (16) to obtain scattering solutions, particularly given
 the proposed SMOS level 2 iterative SSS inversion scheme in
 which the surface wind speed is adjusted until convergence to a
 solution for the salinity is achieved. The proposed solution for
 SMOS level 2 processing involves precomputing the scattered
 celestial noise for a range of wind speeds, incidence angles,
 specular sky locations, and the incidence plane orientation
 angle ψ_{uh} introduced in Part I. The precomputed results are
 stored in a lookup table from which solutions are obtained
 during the salinity inversion procedure by interpolation. The
 change of variables introduced in Part I involving the incidence
 plane orientation angle ψ_{uh} allows the separation of the impact
 of viewing geometry at the target from the impact of specular
 sky location, thereby enabling the creation of a lookup table

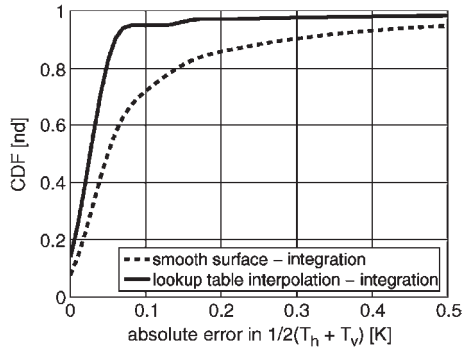


Fig. 11. Cumulative distribution function of the difference between $(1/2(T_h + T_v))$ obtained by interpolation from the lookup table and by the per-measurement computation of the scattering solutions (solid curve). Cumulative distribution function of the difference between $(1/2(T_h + T_v))$ obtained by use of the weighted flat surface reflection model and by the per-measurement computation of the scattering solutions (dashed curve). The differences are shown for the April ascending orbit only, and the geophysical conditions are the same as in Fig. 10. The Kudryavtsev wave spectrum and the KA electromagnetic scattering model are used for both the lookup table generation and the per-measurement integrations.

694 with practical discretizations in all dimensions. For the results
 695 presented in this paper, we have generated scattered celestial
 696 noise solutions for wind speeds of 3, 5, 7, 10, 15, and $25 \text{ m} \cdot \text{s}^{-1}$
 697 on a regular $3.75^\circ \times 3.75^\circ$ grid in specular right ascension and
 698 declination. The grid spacing in ψ_{uh} is 22.5° , and the incidence
 699 angles range from 0° to 60° by 5° and from 60° to 80° by 10° .
 700 To evaluate the performance of this lookup table solution, we
 701 considered the same uniform geophysical conditions as in the
 702 previous section and computed, for each measurement of each
 703 dwell line, the difference between the solution obtained from
 704 numerical integration of (16) and that obtained from multilinear
 705 interpolation from the lookup table. The solid curve in Fig. 11
 706 shows the cumulative distribution function of the absolute dif-
 707 ference between these two computation methods for ascending
 708 swath on April 1, when we expect the worst contamination for
 709 ascending passes. The absolute difference in the unpolarized
 710 signal $(1/2(T_v + T_h))$ is less than 0.1 K in about 95% of
 711 measurements, which is far better than that obtained with the
 712 perfectly smooth surface solution. For comparison, the dashed
 713 curve in the same figure shows the cumulative distribution func-
 714 tion of the difference between the WEF-weighted flat surface
 715 reflection model and the per-measurement integration results.
 716 Similar results were found for the September 28 descending
 717 swath. Therefore, the lookup table approach represents the
 718 per-measurement integration with sufficient fidelity that it is
 719 appropriate for use in an operation processor. Moreover, the
 720 approach easily accommodates alternative scattering models.
 721 The strong directional spreading effect of the rough ocean
 722 surface permits the creation of the lookup table by integration
 723 over a reduced resolution sky map with a grid spacing of
 724 $3.75^\circ \times 3.75^\circ$ in right ascension and declination. Presently, the
 725 rough surface scattering solutions are implemented for wind
 726 speeds greater than $3 \text{ m} \cdot \text{s}^{-1}$. At zero wind speed, the WEF-
 727 weighted smooth surface solution given in (15) is implemented
 728 using the nominal high-resolution sky map (with $0.25^\circ \times 0.25^\circ$
 729 grid spacing and strong sources excluded). For nonzero wind
 730 speeds below $3 \text{ m} \cdot \text{s}^{-1}$, surface roughness spectral descriptions

are known to be inaccurate, and the approach we take to
 estimate the celestial sky glitter contamination in this low wind
 speed range is to linearly interpolate between solutions for the
 perfectly smooth and $3 \text{ m} \cdot \text{s}^{-1}$ rough surfaces. Although this
 approach lacks physical basis, it is proposed here as a practical
 solution in the absence of an adequate rough surface statistical
 description for low surface wind speeds. It is anticipated that the
 algorithm will be refined based on SMOS data obtained after
 launch.

VI. SUMMARY AND DISCUSSION

In this paper, we have examined how the rough sea surface
 scattering of L-band celestial sky radiation might affect SMOS
 measurements.

We began by presenting the nominal celestial sky brightness
 temperature map at L-band that was generated for SMOS
 using an approach similar to that described in [2]. The nom-
 inal map includes the appropriately integrated impact of the
 hydrogen line emission, but the impact of highly localized
 strong sources is neglected. Since omission of these strong
 sources from this nominal sky map may introduce errors into
 the scattering calculations, we also derived a map of strong
 sources and their brightness temperatures using high-resolution
 surveys. We found that, for wind speeds greater $3 \text{ m} \cdot \text{s}^{-1}$ and
 for the two rough surface scattering models (KA and SSA-1)
 considered in this paper, the scattered signals associated with
 these localized strong sources are extremely small owing to
 the directional spreading of the scattered signal by the rough
 surface. Therefore, in the scattering calculations, we neglected
 the impact of such sources.

Next, we established expressions for the expected signals at
 the SMOS antenna array for both flat (perfectly smooth) and
 rough seas. Using an approximate isotropic (in DC coordinates)
 synthetic antenna weighting function (i.e., WEF), we obtained
 expressions for the contribution of the scattered celestial sky
 radiation to the total reconstructed brightness temperatures. In
 theory, to properly assess the impact of celestial glitter in the
 presence of surface roughness on the reconstructed brightness
 temperatures, the scattered noise must be computed over the
 instrument FOV and then integrated over the synthetic antenna
 weighting function. Given the extreme computational burden of
 this approach, we evaluated the impact of computing only the
 synthetic boresight solution and avoiding the WEF integration
 entirely. We found that, in general, the rough surface scattered
 signal is sufficiently smooth that, even in the vicinity of a strong
 (i.e., 50 K) localized source, the scattered signal is not modified
 by more than approximately 0.05 K by integration over the
 WEF, so that this step may be avoided in rough ocean surface
 conditions. Although the WEF impact might be nonnegligible
 for surface roughness at wind speeds lower than $3 \text{ m} \cdot \text{s}^{-1}$ or
 highly heterogeneous rough surfaces, we do not consider it
 except for the perfectly smooth surface conditions.

The sampling characteristics of the instrument are important
 factors in determining the overall impact of scattered celestial
 noise for a particular mission. Both the Aquarius/SAC-D and
 SMOS satellites will maintain sun-synchronous orbits, so that
 the specular reflection of the antenna pattern on the celestial

787 sphere will slowly evolve with time, making one complete
 788 cycle in a year. As compared with Aquarius/SAC-D, the large
 789 FOV of MIRAS is associated with a much larger specular
 790 domain in the celestial sphere, thus the reconstructed brightness
 791 temperatures derived from MIRAS will suffer from a large
 792 range of contamination at any given dwell line on Earth. The
 793 results presented here indicate that the contamination exhibits
 794 a strong seasonal cycle that is different for the ascending and
 795 descending swaths. The largest contamination occurs in the
 796 descending swath in September and October, when the specular
 797 projection of the FOV is aligned with a strip of strong noise
 798 in the vicinity of the galactic equator. The geometry of the
 799 problem is such that contamination patterns tend to be elon-
 800 gated in the along-track direction. Moreover, during one period
 801 of time each year, the specular projections of dwell lines for
 802 both the ascending and descending swaths will be aligned with
 803 the galactic equator, and during this time period, contamination
 804 will be most severe. Considering the flat sea surface reflected
 805 signal alone, a significant fraction of the measurements in many
 806 of the dwell lines will be contaminated by reflected celestial
 807 noise exceeding 4 K in the descending swath during September
 808 and October (and to a large extent in August and November).
 809 Considering moderate wind speed conditions, a larger portion
 810 of dwell lines will suffer from contamination in which surface
 811 roughness modifies the flat surface specularly reflected signal
 812 by more than 0.1 K.

813 Given this potential for strong contamination in a large
 814 fraction of measurements and the computational burden of the
 815 rough surface scattering calculations, we examined a strategy
 816 for computing the rough surface scattered signal using a pre-
 817 computed lookup table expressed in terms of the specular sky
 818 location, incidence angle, wind speed, and the incidence plane
 819 orientation angle ψ_{uh} introduced in Part I. For the monthly
 820 orbits considered here, results obtained by interpolation from
 821 the lookup table differ from per-measurement scattering calcu-
 822 lations by less than 0.1 K in 95% of measurements for April and
 823 September, during which we expect the worst contamination
 824 and the largest impact of surface roughness.

825 In the monthly orbit calculations with a moderate surface
 826 wind speed, only 70% of the rough surface scattered sig-
 827 nals differ from the smooth surface counterparts by less than
 828 0.1 K. Importantly, the numerically integrated scattered signals
 829 are based on asymptotic scattering models, and the statistical
 830 description of the rough surface is based on an idealized wave
 831 model. Although we found that in the vicinity of the strongest
 832 noise source the results obtained from two electromagnetic
 833 models do not differ by more than 0.02 K, the amplitudes and
 834 phases of the wind direction dependence can exhibit large dif-
 835 ferences between models. In addition, we have not considered
 836 here the dependence of the results on the wave model, which
 837 may have a significant impact on the contamination and its
 838 relative wind direction dependence.

839 Finally, we have not considered polarized source radiation.
 840 Recently, new surveys of linearly polarized radiation (i.e., the
 841 third and fourth Stokes parameters) over the northern sky at a
 842 frequency of 1.4 GHz have become available [23]–[26]. These
 843 maps reveal a highly variable polarized intensity that can reach
 844 500 mK in magnitude (e.g., in the vicinity of the North Polar

Spur). This polarization, which is neglected in our formulation, 845
 might impact the celestial noise contamination to an extent that 846
 is significant for SSS retrieval. Unfortunately, incorporation of 847
 this polarization complicates the formulation. In particular, the 848
 polarimetric algorithm must account for polarization rotation 849
 from the celestial basis to the usual target basis as well as 850
 downward Faraday rotation. Generalizing the expression for the 851
 total scattered brightness temperature in the antenna frame (3) 852
 to the fully polarized case, we obtain 853

$$\begin{aligned} \overline{\mathbf{T}}_p^a &= \frac{1}{\Omega_a} \int_{\Omega_a} \frac{(\mathbf{GM}_\alpha)}{4\pi \cos \theta_s} e^{-a \sec \theta_s} \\ &\times \int_{\Omega_0(\Omega_a)} \mathbf{M}_s(\Omega_a, \Omega_0) \mathbf{M}_{fd}(\Omega_0, t) \mathbf{M}_\Psi \mathbf{T}_q e^{-a \sec \theta_0} d\Omega_0 d\Omega_a \end{aligned} \quad (18)$$

where $\mathbf{T}_q = (\mathbf{T}_h, \mathbf{T}_v, \mathbf{U}, \mathbf{V})^T$ is the full Stokes vector of 854
 incidence radiation, and $\overline{\mathbf{T}}_p^a$ is the Stokes vector of the 855
 WEF-weighted signal in the instrument polarization basis. In 856
 contrast with the formulation given in [3], which is appro- 857
 priate for unpolarized sky radiation, $\mathbf{M}_s(\Omega_a, \Omega_0)$ is the fully 858
 polarimetric Mueller matrix (with the obvious dependence on 859
 the rough surface omitted). The incoming Stokes vector \mathbf{T}_q is 860
 transformed before scattering by a change in polarization basis 861
 $\mathbf{M}_\Psi(\Omega_0)$ and the time-dependent Faraday rotation $\mathbf{M}_{fd}(\Omega_0, t)$, 862
 which in turn depends upon the incident radiation direction. 863
 The transformation matrix $\mathbf{M}_\Psi(\Omega_0)$ implicitly depends on the 864
 target location and radiometer incidence and azimuth angles, 865
 but these additional dependencies may be accounted for by the 866
 incidence plane orientation angle ψ_{uh} introduced in Part I, so 867
 that more explicitly $\mathbf{M}_\Psi = \mathbf{M}_\Psi(\psi_{uh}, \Omega_0)$. Therefore, without 868
 Faraday rotation, no additional difficulties are encountered in 869
 the formulation of the lookup table. When we perform the 870
 integration of the fully polarimetric scattering cross sections 871
 over the upper hemisphere for each $\{\alpha_s, \delta_s, \theta_s, \psi_{uh}\}$, the set 872
 of polarization basis rotations (one for each point in the upper 873
 hemisphere integration) is completely determined. In practice, 874
 source polarization may increase the sensitivity of the scattered 875
 Stokes vector components to the orientation angle ψ_{uh} and 876
 therefore require a lookup table with finer resolution than for 877
 the unpolarized case. 878

A more difficult problem involves the downward Faraday 879
 rotation. Were it not for the time dependence in the Faraday 880
 rotation, no additional problem would arise, since the ad- 881
 ditional rotation could be incorporated into the polariza- 882
 tion basis transformation as an additional rotation. However, 883
 Faraday rotation is strongly time dependent, and this neces- 884
 sitates further approximation to be able to use a pregener- 885
 ated time-independent lookup table of scattered noise. One 886
 possible approach is to approximate the downward Faraday 887
 rotation by the time-dependent value evaluated only in the 888
 specular direction. Unfortunately, in general, the scattering 889
 matrix does not commute with the downward Faraday ro- 890
 tation matrix, so that $\mathbf{M}_s(\Omega_a, \Omega_0) \mathbf{M}_{fd}(\Omega_0, t) \neq \mathbf{M}_{fd}(\Omega_0, t)$ 891
 $\mathbf{M}_s(\Omega_a, \Omega_0)$, and thus, it is not possible to bring $\mathbf{M}_{fd}(\Omega_0, t)$ 892

893 outside the integral, even with the time-dependent specular
894 approximation.

895 The effect of Faraday rotation is analogous to the effect
896 of the polarization basis rotation. Without Faraday rotation,
897 the polarization basis rotation is strictly a function of the
898 specular location and incidence plane orientation angle ψ_{uh} , so
899 that it will be accounted for implicitly. Unfortunately, Faraday
900 rotation is an additional (seventh) independent variable. If,
901 however, we neglect the portion of the ψ_{uh} dependence related
902 to variations in the mapping from the upper hemisphere to the
903 sky, then we can adjust ψ_{uh} by the Faraday rotation angle
904 to obtain a new pseudo-orientation angle $\tilde{\psi}_{uh}$ that effectively
905 accounts for Faraday rotation at the expense of properly ac-
906 counting for the (possibly more subtle) effect of sky noise
907 orientation on the upper hemisphere. According to the models
908 considered in this paper, the maximum peak-to-peak variability
909 (with respect to ψ_{uh}) in the scattered unpolarized signal was
910 on order of 0.5 K; therefore, this approach may be worth
911 consideration.

912 APPENDIX 913 GENERATION OF A REDUCED-RESOLUTION 914 CELESTIAL MAP

915 Here, we describe the method that we used to generate a
916 reduced-resolution celestial map, which conserves the energy
917 flux of the full-resolution map.

918 Letting δ denote declination and α right ascension, the
919 original discrete celestial map provides data on a grid of cells
920 such that the brightness temperature field is piecewise constant
921 within each cell and has the form

$$T_{\text{sky}}^f = T_{\text{sky}}^c \left(\delta_0^f + (j^f - 1)(\Delta\delta)^f, \alpha_0^f + (k^f - 1)(\Delta\alpha)^f \right) \quad (\text{A1})$$

922 where j^f and k^f are positive integer indices that satisfy

$$1 \leq j^f \leq n_\delta^f \quad (\text{A2})$$

$$1 \leq k^f \leq n_\alpha^f. \quad (\text{A3})$$

923 Here, the grid spacing is $(\Delta\delta)^f = 0.25^\circ$ in declination and
924 $(\Delta\alpha)^f = 0.25^\circ$ in right ascension. A reduced-resolution celes-
925 tial map was produced by applying an energy-flux-conserving
926 averaging operator $R(\cdot)$ to the original celestial map to
927 produce a celestial noise map on a low-resolution grid
928 $\mathbf{G}_r(j^c(\Delta\delta)^c, k^c(\Delta\alpha)^c)$, where $(\Delta\delta)^c = (2n^c + 1)(\Delta\delta)^f$, and
929 $(\Delta\alpha)^c = (2n^c + 1)(\Delta\alpha)^f$. The integer rescaling factor n^c is
930 set to 7 for this paper, which yields a 15-fold increase in grid
931 spacing in right ascension and declination. The integer indices
932 of the coarse grid, i.e., j^c and k^c , satisfy

$$1 \leq j^c \leq \frac{(n_\delta^f - 1)}{(2n^c + 1)} + 1 \quad (\text{A4})$$

$$1 \leq k^c \leq \frac{(n_\alpha^f - 1)}{(2n^c + 1)} + 1 \quad (\text{A5})$$

and the discrete low-resolution brightness temperature 933
field is 934

$$T_{\text{sky}}^c(j^c, k^c) = \frac{1}{\mathcal{N}} \sum_{j^f=j_0^f}^{j_1^f} \sum_{k^f=k_0^f}^{k_1^f} \sin\left(\delta_0^f + j^f(\Delta\delta)^f\right) \\ \times T_{\text{sky}}^f\left(\delta_0^f + (j^f - 1)(\Delta\delta)^f, \alpha_0^f + (k^f - 1)(\Delta\alpha)^f\right) \quad (\text{A6})$$

where T_{sky}^f is the (piecewise constant) fine grid brightness 935
temperature field, and T_{sky}^c is the coarse grid field. The index 936
limits of summation over the fine grid may be expressed in 937
terms of coarse grid indices and the resolution reduction factor 938
 n^c by 939

$$j_0^f(j^c) = 1 + (2n^c + 1)(j^c - 1) - n^c \quad (\text{A7})$$

$$j_1^f(j^c) = 1 + (2n^c + 1)(j^c - 1) + n^c \quad (\text{A8})$$

$$k_0^f(k^c) = 1 + (2n^c + 1)(k^c - 1) - n^c \quad (\text{A9})$$

$$k_1^f(k^c) = 1 + (2n^c + 1)(k^c - 1) + n^c. \quad (\text{A10})$$

The factor 940

$$\mathcal{N} = \sum_{j^f=j_0^f}^{j_1^f} \sum_{k^f=k_0^f}^{k_1^f} \sin\left(\delta_0^f + j^f(\Delta\delta)^f\right) \quad (\text{A11})$$

is a normalization factor for the averaging operator. The first 941
cell in the reduced grid (in both declination and right ascension) 942
is always aligned with the first cell in each dimension in the 943
original grid, and the celestial brightness temperature values 944
assigned to each of the reduced-resolution grid cells is the 945
weighted average of the brightness temperatures in all original 946
grid cells contained within the encompassing coarse grid cell. 947
In the averaging procedure, the weight given to a particular 948
fine grid cell is proportional to the solid angle subtended by 949
that cell. 950

ACKNOWLEDGMENT 951

The authors would like to thank S. Zine and D. Le Vine 952
for contributing to the SMOS sky map generation and the 953
anonymous reviewers for helping us improve the manuscript. 954
The centrosymmetric weighting function used in the SMOS 955
portion of the analysis was developed by P. Waldteufel. 956

REFERENCES 957

- [1] S. H. Yueh, R. West, W. J. Wilson, F. K. Li, E. G. Njoku, and 958
Y. Rahmat-Samii, "Error sources and feasibility for microwave remote 959
sensing of ocean salinity," *IEEE Trans. Geosci. Remote Sens.*, vol. 39, 960
no. 5, pp. 1049–1060, May 2001. 961
- [2] D. M. Le Vine and S. Abraham, "Galactic noise and passive microwave 962
remote sensing from space at L-band," *IEEE Trans. Geosci. Remote Sens.*, 963
vol. 42, no. 1, pp. 119–129, Jan. 2004. 964

- 965 [3] J. Tenerelli, N. Reul, A. A. Mouche, and B. Chapron, "Earth viewing
966 L-band radiometer sensing of sea surface scattered celestial sky radia-
967 tion. Part I: General characteristics," *IEEE Trans. Geosci. Remote Sens.*,
968 vol. 46, no. 3, pp. xxx-xxxx, Mar. 2008.
- 969 [4] M. Sánchez-Nogales, F. Pironcini, and J. A. G. Abeytua, "Earth Explorer
970 Mission CFI software: Mission conventions document," DEIMOS Space
971 S.L., Madrid, Spain, Jul. 2003. Tech. Note.
- 972 [5] W. Reich, "A radio continuum survey of the northern sky at 1420
973 MHz—Part I," *Astron. Astrophys., Suppl. Ser.*, vol. 48, pp. 219–297,
974 Jul. 1982.
- 975 [6] P. Reich and W. Reich, "A radio continuum survey of the northern sky at
976 1420 MHz—Part II," *Astron. Astrophys., Suppl. Ser.*, vol. 63, pp. 205–292,
977 Jul. 1986.
- 978 [7] P. Reich, J. C. Testori, and W. Reich, "A radio continuum survey of the
979 southern sky at 1420 MHz, the atlas of contour maps," *Astron. Astrophys.*,
980 vol. 376, no. 3, pp. 861–877, Sep. 2001.
- 981 [8] J. C. Testori, P. Reich, J. A. Bava, F. R. Colomb, E. E. Hurrell, J. J. Larrarte,
982 W. Reich, and A. J. Sanz, "A radio continuum survey of the southern
983 sky at 1420 MHz. Observations and data reduction," *Astron. Astrophys.*,
984 vol. 368, no. 3, pp. 1123–1132, Mar. 2001.
- 985 [9] P. M. W. Kalberla, W. B. Burton, D. Hartmann, E. M. Arnal, E. Bajaja,
986 R. Morras, and W. G. L. Pöppel, "The Leiden/Argentine/Bonn (LAB)
987 survey of galactic HI. Final data release of the combined LDS and IAR
988 surveys with improved stray-radiation corrections," *Astron. Astrophys.*,
989 vol. 440, no. 2, pp. 775–782, Sep. 2005.
- 990 [10] D. Hartmann and W. B. Burton, *Atlas of Galactic Neutral Hydrogen*.
991 Cambridge, U.K.: Cambridge Univ. Press, 1997.
- 992 [11] E. M. Arnal, E. Bajaja, J. J. Larrarte, R. Morras, and W. G. L. Pöppel, "A
993 high sensitivity HI survey of the sky at $\delta \leq -25^\circ$," *Astron. Astrophys.*,
994 *Suppl. Ser.*, vol. 142, pp. 35–40, Feb. 2000.
- 995 [12] E. Bajaja, E. M. Arnal, J. J. Larrarte, R. Morras, W. G. L. Pöppel, and
996 P. M. W. Kalberla, "A high sensitivity HI survey of the sky at $\delta \leq -25^\circ$.
997 Final data release," *Astron. Astrophys.*, vol. 440, pp. 767–773, Sep. 2005.
- 998 [13] A. Wright and R. Otrupcek, *Parkes Catalog*. Epping, Australia:
999 Australia Telescope Nat. Facility, 1990.
- 1000 [14] J. J. Condon, W. D. Cotton, E. W. Greisen, Q. F. Yin, R. A. Perley,
1001 G. B. Taylor, and J. J. Broderick, "The NRAO VLA sky survey," *Astron.*
1002 *J.*, vol. 115, no. 5, pp. 1693–1716, May 1998.
- 1003 [15] P. Beckmann and A. Spizzichino, *The Scattering of Electromagnetic*
1004 *Waves From Rough Surfaces*. New York: Macmillan, 1963.
- 1005 [16] A. G. Voronovich, "Small-slope approximation in wave scattering by
1006 rough surfaces," *Sov. Phys.—JETP*, vol. 62, pp. 65–70, 1985.
- 1007 [17] A. Guissard, "Mueller and Kennaugh matrices in radar polarimetry," *IEEE*
1008 *Trans. Geosci. Remote Sens.*, vol. 32, no. 3, pp. 590–597, May 1994.
- 1009 [18] C. Mätzler and P. W. Rosenkranz, "Dependence of microwave brightness
1010 temperature on bistatic surface scattering: Model functions and applica-
1011 tion to AMSU-A," *IEEE Trans. Geosci. Remote Sens.*, vol. 45, no. 7,
1012 pp. 2130–2138, Jul. 2007.
- 1013 [19] D. S. S. L., "Computation of the synthetic antenna directional gain as
1014 interface to L2 processor, synthetic antenna, Apr. 2005, Lisboa, Portugal:
1015 DEIMOS Space S.L. Tech. Note.
- 1016 [20] P. Waldteufel and S. Zine, "Approximating the weighting function to be
1017 used in the SMOS Level 2 processor," CBSA, Toulouse, France, 2005.
1018 Tech. Rep., 32 p..
- 1019 [21] J. Tournadre, B. Chapron, N. Reul, and D. C. Vandemark, "A satellite
1020 altimeter model for ocean slick detection," *J. Geophys. Res.*, vol. 111,
1021 no. C4, p. C04004, 2006.
- 1022 [22] V. N. Kudryavtsev, V. K. Makin, and B. Chapron, "Coupled sea surface-
1023 atmosphere model 2. Spectrum of short wind waves," *J. Geophys. Res.*,
1024 vol. 104, no. C4, pp. 7625–7639, 1999.
- 1025 [23] M. Wollleben, T. L. Landecker, W. Reich, and R. Wielebinski, *An Ab-*
1026 *solutely Calibrated Survey of Polarized Emission From the Northern Sky*
1027 *at 1.4 GHz*, 2005. [Online]. Available: [http://www.citebase.org/abstract?](http://www.citebase.org/abstract?id=oai:arXiv.org:astro-ph/0510456)
1028 [id=oai:arXiv.org:astro-ph/0510456](http://www.citebase.org/abstract?id=oai:arXiv.org:astro-ph/0510456)
- 1029 [24] M. Wollleben, T. L. Landecker, W. Reich, and R. Wielebinski, "An ab-
1030 solutely calibrated survey of polarized emission from the northern sky at
1031 1.4 GHz—Observations and data reduction," *Astron. Astrophys.*, vol. 448,
1032 no. 1, pp. 411–424, Mar. 2006.
- 1033 [25] E. Carretti, S. Poppi, W. Reich, P. Reich, E. Fuerst, G. Bernardi,
1034 S. Corriglioni and C. Sbarra, "Deep 1.4-GHz observations of diffuse po-
1035 larized emission," *Mon. Not. R. Astron. Soc.*, vol. 367, no. 1, pp 132–138,
1036 Mar. 2006. [Online]. Available: [http://www.citebase.org/abstract?id=oai:](http://www.citebase.org/abstract?id=oai:arXiv.org:astro-ph/0512286)
1037 [arXiv.org:astro-ph/0512286](http://www.citebase.org/abstract?id=oai:arXiv.org:astro-ph/0512286)
- 1038 [26] M. Haverkorn, B. M. Gaensler, N. M. McClure-Griffiths, J. M. Dickey,
1039 and A. J. Green, *The Southern Galactic Plane Survey: Polarized Ra-*
1040 *dio Continuum Observations and Analysis*, 2006. [Online]. Available:
1041 <http://www.citebase.org/abstract?id=oai:arXiv.org:astro-ph/0609010>



Nicolas Reul received the B.S. degree in marine 1042
science engineering from Toulon University, Toulon, 1043
France, in 1993 and the Ph.D. degree in physics (fluid 1044
mechanics) from the University of Aix-Marseille II, 1045
Marseille, France, in 1998. 1046

From 1999 to 2001, he was with the Depart- 1047
ment of Applied Marine Physics, Rosenstiel School 1048
of Marine and Atmospheric Science, University of 1049
Miami, Miami, FL, as a Postdoctoral Researcher in 1050
the team of Prof. M. Donelan. Since 2001, he has 1051
been a Research Scientist with the Spatial Oceanog- 1052
raphy Group, Laboratoire d'Océanographie Spatiale, Institut Français de 1053
Recherche et d'Exploitation de la Mer, Plouzané, France, where is responsible 1054
for activities concerning the SMOS satellite mission. The focus of his research 1055
program is the improvement of the understanding of the physical processes in 1056
the air-sea interface and passive/active remote sensing of the ocean surface. 1057
He has experience in applied mathematics, physical oceanography, and electro- 1058
magnetic wave theory and its application to ocean remote sensing. He is a 1059
member of the European Space Agency/SMOS Science Advisory Group. 1060



Joseph Tenerelli received the B.S. degree in 1061
atmospheric sciences from the University of 1062
Washington, Seattle, in 1994. 1063

From 1999 to 2005, he was a Research Asso- 1064
ciate with the Rosenstiel School of Marine and At- 1065
mospheric Science, University of Miami, Miami, FL, 1066
where he was part of a team that developed a coupled 1067
atmosphere-ocean-surface wave model with vortex- 1068
following mesh refinement suitable for simulating 1069
hurricanes. Since April 2005, he has been a Research 1070
Engineer with the Laboratoire d'Océanographie 1071
Spatiale, Institut Français de Recherche et d'Exploitation de la Mer, Plouzané, 1072
France, as part of a team that is developing an algorithm for retrieving sea 1073
surface salinity from L-band radiometric measurements (the European Space 1074
Agency's Soil Moisture and Ocean Salinity project). 1075



Nicolas Floury received the Engineering degree in 1076
telecommunication techniques from the Ecole Na- 1077
tionale Supérieure des Télécommunications, Paris, 1078
France, in 1993 and the Ph.D. degree in physics ap- 1079
plied to remote sensing from the Université Paris 7, 1080
Paris, in 1999. 1081

Since 1999, he has been with the Wave Interaction 1082
and Propagation Group, Electromagnetics and Space 1083
Environments Division, European Space Research 1084
and Technology Centre (ESTEC), European Space 1085
Agency, Noordwijk, The Netherlands. His interests 1086
are in electromagnetic modeling and signal processing applied to the study of 1087
the interaction between microwaves and natural media. 1088



Bertrand Chapron received the B.Eng. degree from 1089
the Institut National Polytechnique de Grenoble, 1090
Grenoble, France, in 1984 and the Ph.D. degree in 1091
physics (fluid mechanics) from the University of 1092
Aix-Marseille II, Marseille, France, in 1988. 1093

He was with the NASA Goddard Space Flight 1094
Center Wallops Flight Facility, Wallops Island, VA, 1095
for three years as a Postdoctoral Research Asso- 1096
ciate. He is currently a Research Scientist and the 1097
Head of the Spatial Oceanography Group, Labora- 1098
toire d'Océanographie Spatiale, Institut Français de 1099
Recherche et d'Exploitation de la Mer, Plouzané, France, where he is responsi- 1100
ble for the Centre ERS Archiving et Traitement. He has been a Coinvestigator 1101
and Principal Investigator in several projects of the European Space Agency 1102
(e.g., ENVISAT and Global Navigation Satellite System), NASA, and Centre 1103
National d'Études Spatiales (e.g., TOPEX/POSEIDON and JASON). He was 1104
also responsible (with H. Johnsen of NORUT) for the ENVISAT ASAR-wave 1105
mode algorithms and scientific preparation for the ENVISAT wind and wave 1106
products. He has experience in applied mathematics, physical oceanography, 1107
and electromagnetic wave theory and its application to ocean remote sensing. 1108